This item is the archived peer-reviewed author-version of:

Tetragonal $Cs_{1.17}In_{0.81}Cl_3$: a charge-ordered indium halide perovskite derivative

Tetragonal Cs1.17In0.81Cl3: a Charge-Ordered Indium Halide Perovskite Derivative

Xiaoyan Tan, Peter W. Stephens, Mylène Hendrickx, Joke Hadermann, Carlo U. Segre, Mark Croft, Chang-Jong Kang, Zheng Deng, Saul H. Lapidus, Sun Woo Kim, Changqing Jin, Gabriel Kotliar, and Martha Greenblatt

Just Accepted

Tetragonal $Cs_{1.17}In_{0.81}Cl_3$: a Charge-Ordered Indium Halide Perovskite Derivative

Xiaoyan Tan,[1,†] Peter W. Stephens,[2] Mylène Hendrickx,[3] Joke Hadermann,[3] Carlo U. Segre,[4] Mark Croft,[5] Chang-Jong Kang,[5] Zheng Deng,[6] Saul H. Lapidus,[7] Sun Woo Kim,[8] Changqing Jin,[6] Gabriel Kotliar,*[,5] Martha Greenblatt*[,1]

[1] Department of Chemistry and Chemical Biology, Rutgers, The State University of New Jersey, Piscataway, New Jersey, 08854, United States

[2] Department of Physics and Astronomy, State University of New York, Stony Brook, New York 11794, United States

[3] EMAT, University of Antwerp, Groenenborgerlaan 171, B-2020 Antwerp, Belgium

[4] Department of Physics and CSRRI, Illinois Institute of Technology, Chicago, Illinois, 60616, United States

[5] Department of Physics and Astronomy, Rutgers, The State University of New Jersey, Piscataway, New Jersey, 08854, United States

[6] Institute of Physics, School of Physics, University of Chinese Sciences, Chinese Academy of Sciences, P. O. Box 603, Beijing, 100190, P. R. China

[7] Advanced Photon Source, Argonne National Laboratory, Argonne, Illinois, 60439, United States

[8] Department of Chemical Education, Chosun University, Gwangju, 61452, South Korea

Corresponding authors' e-mail: greenbla@chem.rutgers.edu and kotliar@physics.rutgers.edu

† Current address: Department of Chemistry and Biochemistry, George Mason University, Virginia, 22030, United States

Abstract

Polycrystalline samples of $Cs_{1.17}In_{0.81}Cl_3$ were prepared by annealing a mixture of CsCl, InCl, and InCl3, stoichiometric for the targeted $CsInCl_3$. Synchrotron powder X-ray diffraction refinement and chemical analysis by EDAX indicated that $Cs_{1.17}In_{0.81}Cl_3$, a tetragonal distorted perovskite derivative ($I4/m$) is the thermodynamically stable product. The refined unit cell parameters and space group were confirmed by electron diffraction. In the tetragonal structure, In^+ and In^{3+} are located in four different crystallographic sites, consistent with their corresponding bond lengths, respectively. In1, In2, In3 are octahedrally coordinated, whereas In4 is at the center of a pentagonal bipyramid of Cl due to the noncooperative octahedral tilting of $In4Cl_6$. The charged-ordered In^+ and In^{3+} was also confirmed by X-ray absorption and Raman spectroscopy. $Cs_{1.17}In_{0.81}Cl_3$ is the first example of an inorganic halide double perovskite derivative with charged ordered In^+ and In^{3+}. Band structure and optical conductivity calculations were carried out with both Generalized Gradient Approximation (GGA) and modified Becke-Johnson (mBJ) approach; the GGA calculations estimated the band gap and optical band gap to be 2.27 eV, and 2.4 eV, respectively. These values are larger with mBJ calculations. The large and indirect band gap suggests that $Cs_{1.17}In_{0.81}Cl_3$ is not a good candidate for photovoltaic application.

Introduction

Recently, inorganic halide perovskites and related compounds have gained attention due to their promising application in optoelectronic devices such as photodetectors, solar cells, light-emitting diodes, semiconductor lasers, etc.[1-9] In particular, cesium-based halide perovskites with formula $CsMX_3$ (M = Pb, Sn; X = Cl, Br, I) have shown exceptional optoelectronic properties. $CsPbI_3$ quantum dots have been incorporated into solar cells which display a power conversion efficiency of 10.77%.[10] The efficiency can be further increased to 11.33% in $CsPb_{0.9}Sn_{0.1}IBr_2$ by substituting Pb with Sn, and I with Br.[11] The highest

efficiency of solar cells based on $CsPbI_3$ quantum dot films reaches 13.45%, which is the highest among all quantum-dot-based solar cells.[12] $CsPbBr_3$-based green light-emitting diodes exhibit a high electroluminescence quantum efficiency of 10.4%, the highest in all perovskite green light-emitting diodes.[13]

Due to the outstanding properties of $CsPbX_3$, but the toxicity of Pb, both experimental and theoretical scientists are searching for alternative inorganic halide perovskites. Filip et al. used computational screening methods and explored the possible cesium metal halide perovskites with other divalent metal ions such as Mg^{2+}, V^{2+}, Mn^{2+}, Ni^{2+}, Cd^{2+}, Hg^{2+}, Ga^{2+}, and In^{2+}.[14] The proposed $CsInCl_3$ and $CsInBr_3$ compounds are of interest, because of the unusual 2+ valence state of In, which has not been reported so far. Later, Körbel et al. also carried out extensive density functional theory (DFT) calculations to explore novel inorganic perovskites and identified $CsInCl_3$ and $RbInBr_3$, as small gap semiconductors.[15] More recent work by Kang and Kotliar studied systematically the structures of $AInX_3$ compounds (A = alkali metals, X = F or Cl) and identified the low lying structures of these materials, and showed that $CsInCl_3$ should be thermodynamically stable and thus should form, providing further motivation for our studies.[16] Recent experimental study of the similar compound $CsTlX_3$ (X = F, Cl) found that Tl disproportionates into Tl^+ and Tl^{3+}.[17] Therefore, we expected that In might disproportionate into In^+ and In^{3+} in $CsInCl_3$ as well. To explore the existence of $CsInCl_3$ compound, its crystal structure, and the oxidation states of In, we embarked on the experimental work to synthesize and investigate the properties of $CsInCl_3$.

Another motivation for studying $CsInCl_3$ arises from its possible superconductivity, observed in related compounds. An example is the well-known perovskite $BaBiO_3$, an insulator with mixed valence Bi^{3+} and Bi^{5+}, which becomes superconducting by hole doping in $Ba_{0.6}K_{0.4}BiO_3$, and $BaBi_{0.7}Pb_{0.3}O_3$, due to the strongly phonon-coupled bands across the Fermi level.[18-19] $CsTlX_3$ have the same valence electron count as $BaBiO_3$, which are expected to show a similar band structure.[20] Theoretical calculations predict the superconducting critical temperature of doped $CsTlF_3$ and $CsTlCl_3$ to be ~30 K and ~20 K, respectively.[21] Although experimental work on $CsTlX_3$ has not discovered superconductivity in these phases so far, it is of interest to explore analogous $CsInCl_3$ for future discovery.

In this manuscript, we report that polycrystalline $Cs_{1.17}In_{0.81}Cl_3$ can be prepared by conventional solid-state techniques. The crystal structure has been determined by X-ray and electron diffraction. The space group is $I4/m$, a distorted derivative of cubic perovskite (Fig. 1). The oxidation state of In is revealed by X-ray absorption spectroscopy. The band gap is determined by first-principles calculations and compared with literature results.[14-15]

Experimental Methods

Starting Materials and Synthesis. The nominal $CsInCl_3$ phase was prepared by conventional solid state methods, similar to ones used for tetragonal $CsTlCl_3$ ($I4/m$),[17] with anhydrous CsCl (wt.99.9%, Alfa Aesar), InCl (wt. 99.995%, Alfa Aesar), and $InCl_3$ (wt. 99.999%, Alfa Aesar). The starting materials were mixed in the ratio of $CsCl: InCl: InCl_3 = 2: 1: 1$, ground thoroughly and loaded into a silica tube which was sealed under vacuum ($< 10^{-2}$ mbar). The ampule was ramped up to 923 K within 24 hours, kept at this temperature for 24 hours, and then cooled down to room temperature over the course of 24 hours. All sample preparations were carried out in an Ar-filled glove box with O_2 and H_2O concentration below 1 ppm.

Laboratory and Synchrotron Powder X-ray Diffraction (SPXD). Samples were measured in the 2θ range from 10° to 80° and collected for 1h on a Bruker D8 Advance Diffractometer (Cu Kα, λ = 1.5418 Å) with a SOL-X solid state detector. Room temperature SPXD (λ = 0.412723 Å) was collected in the 2θ range from 0.5° to 50° at the 11-BM-B beam line at the Advanced Photon Source (APS), Argonne National Laboratory. Diffraction data analysis and Rietveld refinement were performed with TOPAS-Academic.[22]

Chemical Analysis. The chemical composition of the samples was determined by energy dispersive X-ray (EDX) analysis with a JEOL 5510 scanning electron microscope (SEM) equipped with an INCA system (Oxford Instruments). Sample preparation was carried out in the glove box to avoid contact with air. The powder was gently smeared out over carbon tape, which was mounted on a metal stub. The stub was transported to the SEM instrument in a protective Ar atmosphere. During insertion, the sample had to be exposed to air for a short while (maximum 5 minutes). Cs-L, In-L and Cl-K lines were used for the composition quantification.

A separate chemical composition analysis was performed on a FEI Osiris transmission electron microscope (TEM), operated at 200 kV equipped with a Super-X detector. A vacuum transfer holder was used to avoid contact with air, and the Cs-L, In-L and Cl-K lines were used for the composition quantification.

Electron Diffraction. The samples for the TEM analysis were prepared in the glove box by crushing the powder of the sample and gently depositing the dry powder on a copper grid covered with a holey carbon film. The sample was transported to and inserted into the TEM without contact with air with a vacuum transfer holder. Selected area electron diffraction (SAED) patterns were performed with a FEI Tecnai G2 TEM.

Thermogravimetric Analysis (**TGA**) **and Differential Scanning Calorimetry (DSC).** A powder sample of about 25 mg was loaded into an alumina crucible in a SDT Q600 TA Instrument and measured between room temperature and 1000 °C at a heating and cooling rate of 10 °C/min under argon flow

X-ray Absorption Spectroscopy (XAS). XAS data were collected at the indium K-edge in fluorescence at the Materials Research Collaborative Access Team (MRCAT)[23] insertion device beam line (Sector 10-ID) on a powder-filled Kapton capillary at room temperature. Data were normalized and background subtracted with Athena and IFEFFIT.[24-25] White line intensities were obtained with Fityk[26] with a Gaussian peak function plus an arctangent step (constrained to the peak energy).

Raman Spectroscopy. Micro Raman measurements have been carried out with an inVia Raman Microscope (Renishaw) and exciting with a solid-state laser (λ_{exc} = 532nm).

DFT calculations. The all-electron full-potential linearized augmented plane-wave (FLAPW) method implemented in WIEN2k[27] was adopted to calculate the electronic structure. Generalized Gradient Approximation (GGA) functional[28] was chosen to calculate the electronic structure. Since GGA underestimates a band gap, we used the modified Becke-Johnson (mBJ) exchange potential[29] in order to determine the precise band gap. A 17 x 17 x 17 k-mesh was used for the Brillouin zone integration and the plane-wave cutoff was $R_{mt} K_{max}$ = 7 in the calculations.

Results and Discussion

Chemical Analysis and Crystal Structure. A polycrystalline light-yellow product was obtained and powder X-ray diffraction (PXD) analysis confirmed the major phase to be "CsInCl$_3$" with ~ 5% of Cs$_2$InCl$_5$·H$_2$O impurity. The sample is hygroscopic, and the color of sample becomes darker when it is exposed to air. Numerous efforts to synthesize CsInF$_3$ and RbInCl$_3$ with similar approach at different temperatures failed to yield the targeted phases.

SEM-EDX and TEM-EDX measurements were carried out to investigate the chemical composition of the "CsInCl$_3$"product. Both EDX studies clearly confirm the presence of the Cs, In, and Cl elements (representative spectrum in Fig. S1). The TEM-EDX study of 20 different crystals reveals a molar ratio of Cs:In:Cl = 0.26(2):0.18(1):0.56(2), which is close to the target of 1:1:3, but with an excess of Cs and less In. This is equivalent to a Cs/In ratio of 1.44 ± 0.14. These results are also confirmed by a statistical SEM-EDX study taken from 50 different crystals, which shows a molar ratio of Cs:In:Cl = 0.23(2):0.16(1):0.60(2) with a Cs/In ratio equal to 1.44 ± 0.16. Thus the chemical analysis indicates that the composition of the material produced is a Cs rich, In deficient phase, of formula, Cs$_{1.17}$In$_{0.81}$Cl$_3$. We speculate that the difference from stoichiometry is not an intrinsic property of the nominal CsInCl$_3$ phase, but due to unknown side reaction(s).

The SPXD of Cs$_{1.17}$In$_{0.81}$Cl$_3$ sample is very similar to that of CsTlCl$_3$, and indeed, initial Rietveld refinement results indicate that it is isostructural with tetragonal CsTlCl$_3$.[17] In this structure, shown in Fig. 1, there are two Cs sites, four In sites, and seven Cl sites. The SEM-EDX results imply that there must be a significant amount of Cs in the nominal In sites, discussed below. Isotropic thermal parameters were refined independently for each site, except for those of the Cl sites, which had a common thermal factor. The Rietveld fit is shown in Fig. 2 and the refined crystallographic data are summarized in Table 1. Details of the refinement, including raw data and computed fit, have been deposited as a cif file in inorganic crystal structure database with CCDC number 1877027.
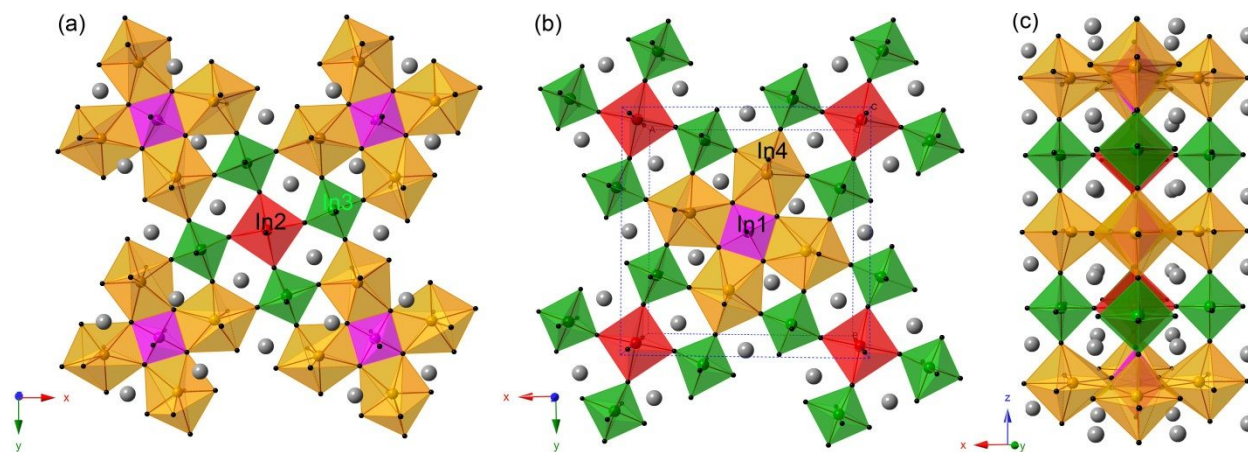

Figure 1. Crystal structure of Cs$_{1.17}$In$_{0.81}$Cl$_3$ with space group $I4/m$. (a) is the xy layer at $z = 0$; (b) is the xy layer at $z = \frac{1}{2}$; (c) is a perspective view of the structure viewed along the y axis. Color code: In1 = magenta, In2 = red, In3 = green, In4 = orange, Cs = grey, and Cl = black.

Two of the nominal In sites, In1 and In3, are octahedrally coordinated, with In-Cl distances between 2.50-2.64 Å, close to the value expected for the In^{3+}-Cl^- distances based on Shannon sum of radii (2.61Å). The calculated bond valence sum of In1 and In3 are 3.06 and 3.14, respectively.[30] Therefore, the charge of In on In1 and In3 sites can be assigned to 3+. The observed In^{3+}-Cl^- distances are also consistent with distances in $Cs_3In_2Cl_9$ (2.41-2.65Å)[31] and $Cs_2InCl_5 \cdot H_2O$ (2.47-2.71Å).[32]

The remaining two nominal In sites have significantly longer In-Cl bond distances (3.00-3.55Å), indicating a lower oxidation state on In2 and In4 sites. Based on the similar bond distances between $Cs_{1.17}In_{0.81}Cl_3$ and $CsTlCl_3$ (Table 2), one would conclude that In^+ occupies In2 and In4 sites, similar to the case of Tl^+ on Tl2 and Tl4 sites. Although the Shannon radius of In^+ is not assigned, the estimated In^+-Cl^- distance should be close to the expected Tl^+-Cl^- distance (3.31Å) for 6-coordinated environment, which agrees with In^+-Cl^- distances in $Cs_{1.17}In_{0.81}Cl_3$. The observed In^+-Cl^- distances are also comparable with those in red InCl (2.87-3.26Å) and yellow InCl (2.90-3.53 Å).[33] In2 is octahedrally coordinated, whereas In4 is at the center of a pentagonal bipyramid of Cl. It is therefore not surprising that $In4^+$-Cl^- distances (3.05 – 3.55 Å) are longer than those of $In2^+$-Cl^- (3.00 – 3.02 Å). The long $In4^+$-Cl^- distances are also observed in the mixed-valence compound, In_5Cl_9, where the average In^+-Cl distance is 3.58Å.[34] Thus, there is In^+/In^{3+} charge order, not In^{2+} in $Cs_{1.17}In_{0.81}Cl_3$, similar to that of Tl^+/Tl^{3+} in $CsTl^+_{0.5}Tl^{3+}_{0.5}Cl_3$.

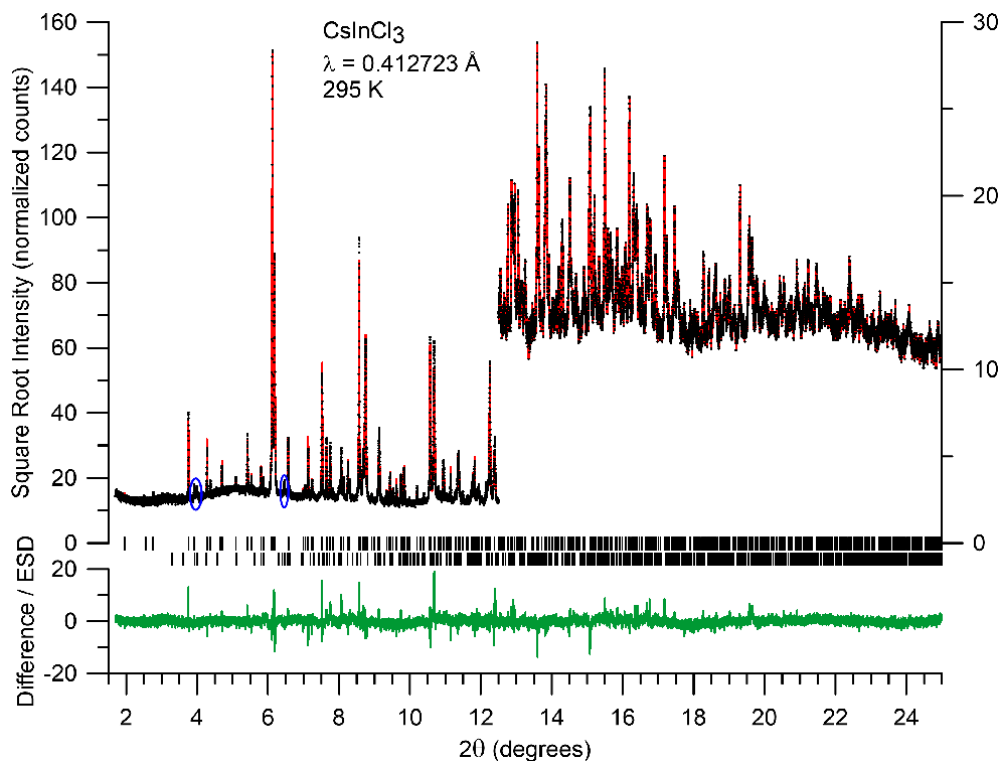**Figure 2.** Rietveld refinement of synchrotron powder X-ray diffraction pattern of $Cs_{1.17}In_{0.81}Cl_3$, including ~ 5% of $Cs_2InCl_5 \cdot H_2O$ impurity. Black dots are the observed pattern, red line is the calculated pattern, vertical black bars are the Bragg positions of $Cs_{1.17}In_{0.81}Cl_3$ (upper row) and $Cs_2InCl_5 \cdot H_2O$ impurity (lower row), and the green line is the difference between observed and calculated patterns. The most visible peaks of the impurity phase are circled in blue.

We now turn to the occupancy of the metal sites. If only In is placed in the In sites, refined occupancies in three of the sites are essentially unity, and 0.93 ± 0.01 in site In2, for a sample composition of $CsIn_{0.996}Cl_3$. This refinement is presented as Model I in Table S1. However, the EDX results imply that there must be a significant amount of Cs in sites which are nominally In. X-ray diffraction essentially measures the total number of electrons (not just valence) in each atomic site, and so the Rietveld refinements are consistent with the replacement of unit occupancy of In by a fraction x Cs, $(1 - 55/49\ x)$ In, and $(1 - 6/49\ x)$ vacancies. (These estimates based on atomic number are borne out by refinements with the full atomic form factors, and they are not significantly affected whether one uses tabulated form factors for neutral atoms or ions.) If we assume that Cs^+ only goes into the In^+ sites, *i.e.*, In2 and In4, and seek to substitute enough Cs for In to account for the observed ratio of Cs:In, 1.44 ± 0.14, the problem of occupancy of sites In2 and In4 is still undetermined. The allowed parameter space, including standard uncertainties of the EDX and x-ray refinements, is illustrated in Fig. S2. Table I describes a refinement of Model II for a composition, $Cs_{1.17}In_{0.81}Cl_3$ with an equal ratio of Cs to In in each of the 1+ sites, 0.536, and a total ratio of Cs to In of 1.44; other assignments of occupancies, consistent with the parameters in Fig. S2, give Rietveld fits that are essentially indistinguishable. The consequent vacancies in sites In2 and In4 (11% and 3%, respectively) create an apparent valence charge imbalance. The most plausible solution is that some fraction of the In in those sites must be In^{3+} instead of In^{1+}.

In the tetragonal *ab* plane, $In2Cl_6$ octahedra corner-share by four $In3Cl_6$ octahedra in four-fold axis symmetry, while $In1Cl_6$ octahedra edge-share with $In4Cl_7$ pentagonal bipyramid in the same fashion. Then these two symmetric segments are connected by corner-sharing $In3Cl_6$ octahedra and $In4Cl_7$ pentagonal bipyramid. Layers centered with $In2Cl_6$ and $In1Cl_6$ octahedra are shown in Fig. 1a and 1b, respectively. These two layers alternate every half a unit cell along the tetragonal *c* axis with corner-sharing connection (Fig. 1c). The fully occupied A-site Cs atoms locate in the space between these $In1Cl_6$, $In2Cl_6$, $In3Cl_6$, and $In4Cl_7$ polyhedra.

Table 1. Refined crystallographic data of $Cs_{1.17}In_{0.81}Cl_3$, according to Model II described in the text.

Compound	$Cs_{1.17}In_{0.81}Cl_3$					
Chemical formula, Mol. Wt.	$Cs_{1.17}In_{0.81}Cl_3$, 354.20					
X-ray wavelength	$\lambda = 0.412723$ Å					
Lattice dimensions, unit cell volume	$a = b = 17.1098(1)$ Å, $c = 11.0523(1)$ Å, $\alpha = \beta = \gamma = 90°$. 3235.50(5) Å^3					
Space group	$I4/m$, #87					
Z	20					
Rietveld criteria of fit for powder diffraction refinements. [a]	$\chi^2 = 2.77$, $R_{wp} = 9.85\%$, $R_p = 7.43\%$, $R_{exp} = 5.91\%$, $R_{Bragg} = 5.21\%$					
Parameters refined	62					
Parameter restraints[b]	9					
Nominal Atom, (valence charge)	Site multiplicity, Wyckoff symbol,	x	y	z	Fractional Occupancy Model II	B_{iso}
Cs1 (+1)	4d	0	½	¼	1	5.7(2)
Cs2 (+1)	16i	0.2108(1)	0.1091(1)	0.2773(1)	1	4.64(5)

In1 (+3)	2a	0	0	0	In: 1	1.4(1)
In2 (+1)	2b	½	½	0	In: 0.577(7) Cs: 0.309(4)	5.4(3)
In3 (+3)	8h	0.4073(2)	0.1966(2)	0	In: 1	2.32(6)
In4 (+1)	8h	0.0837(2)	0.2589(2)	0	In: 0.629(3) Cs: 0.337(2)	5.1(4)
Cl1 (-1)	4e	0	0	0.227(1)	1	3.27(7)
Cl2 (-1)	16i	0.0926(4)	0.3073(4)	0.2688(4)	1	3.27(7)
Cl3 (-1)	8h	0.1372(5)	0.0586(6)	0	1	3.27(7)
Cl4 (-1)	8h	0.3771(6)	0.0524(7)	0	1	3.27(7)
Cl5 (-1)	8h	0.2616(6)	0.2470(7)	0	1	3.27(7)
Cl6 (-1)	8h	0.1529(7)	0.4539(7)	0	1	3.27(7)
Cl7 (-1)	8h	0.4579(8)	0.3297(6)	0	1	3.27(7)

a. $R_{wp} = \sqrt{\dfrac{\sum_i w_i (y_i^{calc} - y_i^{obs})^2}{\sum_i w_i (y_i^{obs})^2}}$, $R_{exp} = \sqrt{\dfrac{N - P}{\sum_i w_i (y_i^{obs})^2}}$, $R_p = \sqrt{\dfrac{\sum_i (y_i^{calc} - y_i^{obs})^2}{\sum_i (y_i^{obs})^2}}$, $\chi^2 = (R_{wp}/R_{exp})^2$, where y_i^{calc} and y_i^{obs} are

the calculated and observed intensities at the ith point in the profile, the weight w_i is $1/\sigma^2$ from counting statistics, with the same normalization factor, N is the number of points in the measured profile and P is the number of refined parameters. R_{exp} is the expected value of R_{wp} if the only deviation of the data from the model is due to statistical errors.

b. All Cl thermal parameters were restrained to be equal, plus three restraints on In:Cs vacancy composition of In2 and In4 sites.

Table 2. Selected bond distances in $Cs_{1.17}In_{0.81}Cl_3$ and Tl-Cl bond distances in $CsTlCl_3$[17]. For each metal atom, bonds are listed in order of increasing length.

| Cs-Cl distances (Å)		In-Cl distances (Å)		Tl-Cl[17] distances (Å)	
Cs1-Cl4	3.59(1) × 4	In1-Cl1	2.50(1) × 2	Tl1-Cl3	2.45(3) × 4
Cs1-Cl2	3.66(1) × 4	In1-Cl3	2.55(1) × 4	Tl1-Cl2	2.56(3) × 2
Cs1-Cl6	3.89(1) × 4	In2-Cl7	3.00(1) × 4	Tl2-Cl1	2.99(3) × 2
Cs2-Cl3	3.42(1)	In2-Cl1	3.02(1) × 2	Tl2-Cl7	3.07(3) × 4
Cs2-Cl5	3.51(1)	In3-Cl7	2.44(1)	Tl3-Cl7	2.39(3)
Cs2-Cl6	3.56(1)	In3-Cl6	2.49(1)	Tl3-Cl2	2.62(1) × 2
Cs2-Cl7	3.64(1)	In3-Cl4	2.52(1)	Tl3-Cl4	2.69(3)
Cs2-Cl2	3.69(1)	In3-Cl2	2.56(1) × 2	Tl3-Cl6	2.71(3)
Cs2-Cl2	3.83(1)	In3-Cl5	2.64(1)	Tl3-Cl5	2.84(3)
Cs2-Cl7	3.93(1)	In4-Cl5	3.05(1)	Tl4-Cl5	2.82(3)
Cs2-Cl2	3.95(1)	In4-Cl4	3.08(1)	Tl4-Cl4	2.93(3)
Cs2-Cl5	3.97(1)	In4-Cl2	3.09(1) × 2	Tl4-Cl2	3.01(1) × 2
Cs2-Cl1	4.10(1)	In4-Cl3	3.20(1)	Tl4-Cl3	3.26(3)
Cs2-Cl4	4.29(1)	In4-Cl6	3.54(1)	Tl4-Cl6	3.45(3)
		In4-Cl3	3.55(1)	Tl4-Cl3	3.55(3)
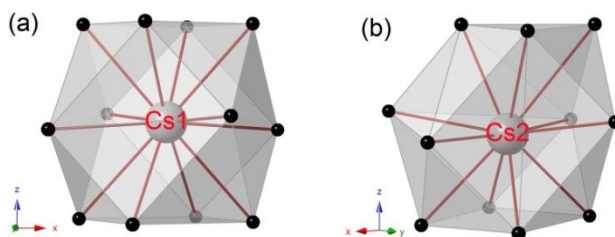
Figure 3. Coordination environment for Cs1 (a) and Cs2 (b) in $Cs_{1.17}In_{0.81}Cl_3$.

One interesting feature of $Cs_{1.17}In_{0.81}Cl_3$ is that the $In4^+$ is seven-coordinated with Cl^- and forms an $In4Cl_7$ pentagonal bipyramid. The irregular coordination environment and the long bond distances for In^+ may be attributed to the almost doubly filled In 5s atomic orbital as shown in the study of binary indium bromides.[35-37] Interestingly the lone pair $5s^2$ electrons of $In2^+$ are not stereo-active, while those of $In4^+$ appear to be active; lone pair distortion can be switched on or off by the environment and does not always distort in its vicinity. If we disregard for the moment the nonstoichiometric composition and presence of Cs in the In sites, nominal "$CsIn^+_{0.5}In^{3+}_{0.5}Cl_3$" could be understood as "$Cs_2In^+In^{3+}Cl_6$", a modified form of double perovskite halide with B site charge order in the formula of $A_2BB'X_6$.[38] In the double perovskite, the three-dimensional (3D) framework is formed by corner-sharing BX_6 and $B'X_6$ octahedra, with A site atoms occupying the cubo-octahedral void of the 3D structure. The modified double perovskite tetragonal structure ($I4/m$) of $Cs_{1.17}In_{0.81}Cl_3$ stems from the ~45° rotation in the ab plane of one fifth of the $B'X_6$ octahedra ($In1Cl_6$) in the double perovskite structure.[39] This $In1Cl_6$ rotation results in the change of adjacent In4 site coordination environment from $In4Cl_6$ octahedra to $In4Cl_7$ pentagonal bipyramid, with long In4-Cl bond distances. Moreover, edge-sharing is created between $In1Cl_6$ and $In4Cl_7$. The interruption of connected corner-sharing caused by $B'X_6$ octahedra rotation is defined as a noncooperative octahedral tilting (NCOT) in double perovskites.[40] Other examples in halides with tetragonal structure ($I4/m$) include β-K_2KAlF_6, low temperature Rb_2KCrF_6, and β-Rb_2KGaF_6, in which the K ions on the B site are also coordinated with seven F atoms and form pentagonal bipyramids.[39, 41] NCOT also have been reported in oxides and oxyfluorides.[42-44] In the modified double perovskite structure of $Cs_{1.17}In_{0.81}Cl_3$, the environment of A site ions are also changed: Cs1 still remains in the cubo-octahedral geometry, but Cs2 connects with eleven Cl and forms an irregular polyhedron (Fig. 3).

Electron Diffraction

To confirm the refined crystal structure based on SPXD data, selected area electron diffraction (SAED) patterns of $Cs_{1.17}In_{0.81}Cl_3$ sample are taken from different zone axes ([100], [001], [$\bar{2}$10], [$\bar{1}\bar{1}$3]/[13$\bar{5}$], [35$\bar{3}$] and [4$\bar{2}\bar{5}$]) (Fig. 4). All SAED patterns could be indexed with the tetragonal cell parameters: a = b ≈ 17.11, c ≈ 11.052 Å and α, β, γ = 90°, and correspond to the following reflection conditions: hkl: $h+k+l = 2n$; $hk0$: $h+k = 2n$; $0kl$: $k+l = 2n$; $0k0$: $k = 2n$.

To check the reflection condition $00l$ (whether it is $l = 2n$ or $l = 4n$), two tilt series of SAED patterns were obtained along the c-axis, shown in Figs. S3 and S4. The intensity of the reflections $00l$: $l=2n$ stays strong during the whole tilt series, indicating that they are not caused by double diffraction and thus do not correspond to $00l$: $l = 4n$. According to the reflection conditions and cell parameters, the possible space groups are $I4$, $I\bar{4}$, $I4/m$, $I422$, $I4mm$, $I\bar{4}2m$, $I\bar{4}m2$ or $I4/mmm$.

Based on very clear intensity distributions in the reflections, all space groups with Laue Class 4/mmm can be excluded. Here, we use the magnified experimental SAED pattern of zone axis [001] to justify this (Fig. 5). In Fig. 5, the projected positions of planes perpendicular to <a> and <110> directions and 2-fold axes along <a> and <110> are drawn. If these are mirror planes or two fold axes for the structure, the reflections connected by these symmetry elements should have equivalent intensities. It is clear that the intensity distribution of the reflections does not satisfy any of these symmetry elements. Therefore, this disagreement rules out all space groups with Laue Class 4/mmm, i.e. $I422$, $I4mm$, $I\bar{4}2m$, $I\bar{4}m2$ or $I4/mmm$.
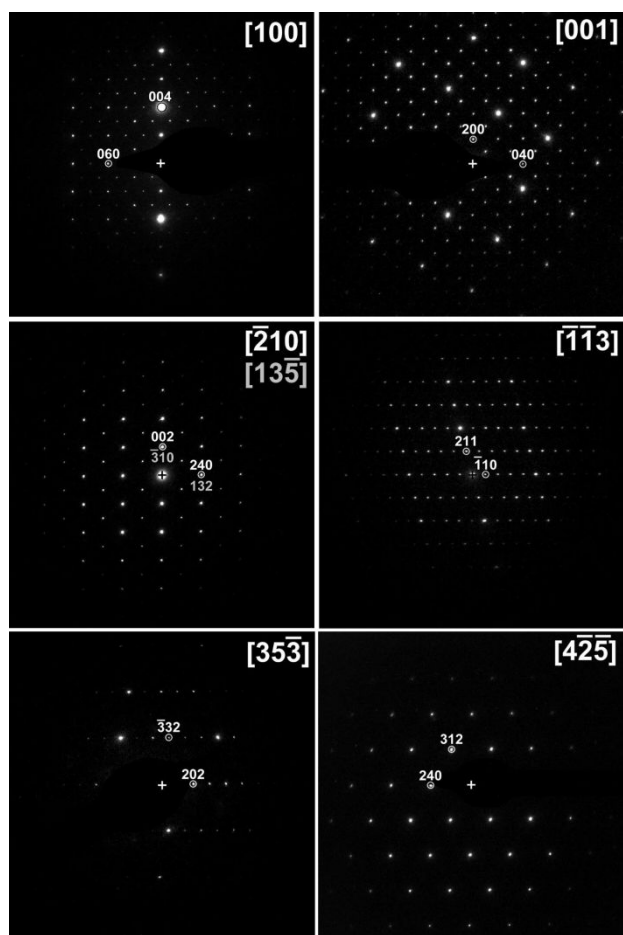

Figure 4. SAED patterns of the $Cs_{1.17}In_{0.81}Cl_3$ sample along the zone axes [100], [001], [$\bar{2}$10], [$\bar{1}\bar{1}$3]/[13$\bar{5}$], [35$\bar{3}$] and [4$\bar{2}$$\bar{5}$].
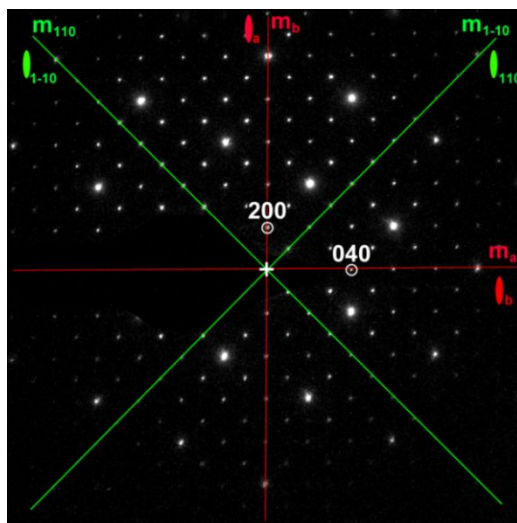
Figure 5. Magnified SAED pattern of zone axes [001]. The mirror plane perpendicular to x is indicated by 'mx' and the 2-fold axis along x by an elliptical shape with index 'x'.

Sample Stability. The stability of the $Cs_{1.17}In_{0.81}Cl_3$ phase was determined by thermogravimetric analysis (TGA) and differential scanning calorimetry (DSC) between 300 and 1273 K under Ar flow. $Cs_{1.17}In_{0.81}Cl_3$ is thermally stable below 600 K without any phase transition or melting under the inert environment (Fig. 6), however the sample mass drops as the temperature increases from 600 K to 1273 K. The mass drop between 600 and 900 K is probably due to sample melting. After 900 K, an endothermal peak shown in the DSC curve at 910 K indicates possible decomposition. The TGA-DSC curves are similar to those of tetragonal $CsTlCl_3$, which is thermally stable up to 623-673 K, the temperature where that phase also starts melting.
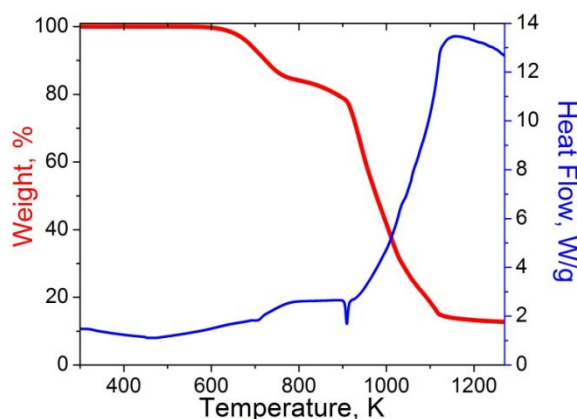

Figure 6. TGA-DSC measurement of $Cs_{1.17}In_{0.81}Cl_3$ between 298 K and 1273 K.

X-ray Absorption Spectroscopy (XAS). As a p-block element, the frontier bonding orbitals of In are the 5p/5s -states with the configurations: In^0-s^2p^1, In^{1+}-s^2p^0 (reflecting the inert pair effect) and In^{3+}-s^0p^0. X-ray absorption edges with final states in the p-valence orbitals can be used to probe the valence/configuration of such p-block elements. In Figure 7a, the In-K near edge spectrum of the $Cs_{1.17}In_{0.81}Cl_3$ is shown along with the standards: elemental-In^0; In^{1+}, InCl; and In^{3+}, $InCl_3$ and In_2O_3.
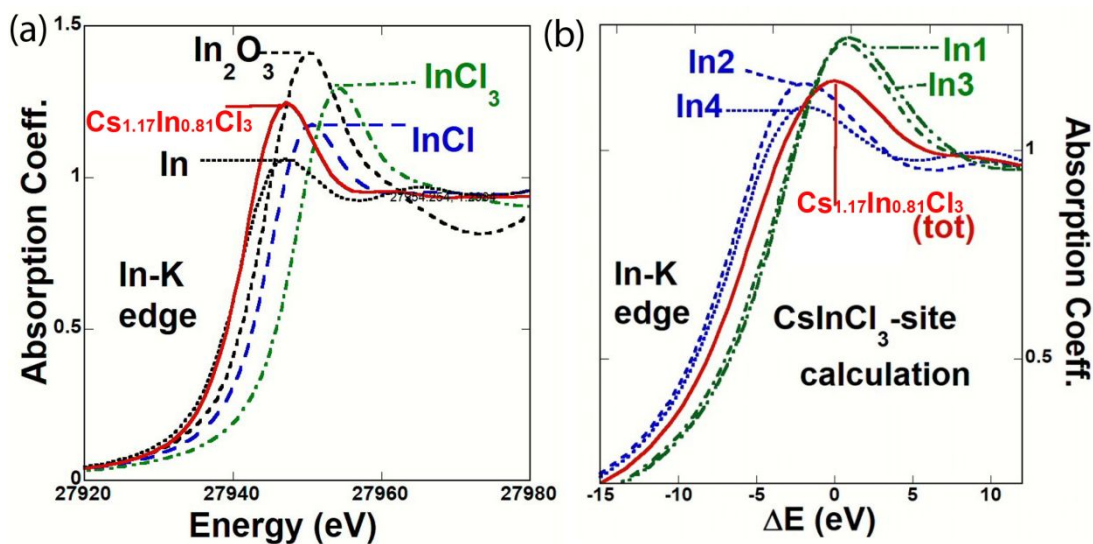
Figure 7. **(a)** A comparison of the In-K edges of $Cs_{1.17}In_{0.81}Cl_3$ to those of the standards: In^0, In-metal; In^{1+}, InCl; In^{3+}, $InCl_3$ and In_2O_3. **(b)** A FEFF 8.4 modeling[45] of the In-K edges at the individual In1, In2, In3, and In4 sites as well as the all-site total $Cs_{1.17}In_{0.81}Cl_3$ spectrum. The energy ΔE is given relative to the all-site WL-peak value.

The In-K near edge spectra are dominated by a strong "white-line" (WL) peak-feature due to 2s-core transitions into empty 5p states. This WL feature rides upon a step-feature due to the onset of transitions into the continuum. Typically, two points regarding the In-valence/WL-feature coupling should be noted: first, the increase in WL-intensity with increasing valence, and second, the chemical shift of the WL to higher energy is not always consistent with increasing valence.[46-48] The chemical shifts in these materials appears to be too structure/ligand dependent for reliable interpretation, so the WL-area will be focused upon.

The increased WL-intensity, with increasing valence, is due partially to the increase of available empty p-final states (e.g. between the In^0 and In^{1+} states), and partially due to the increased transition matrix element via the increased localization of the p-final states upon loss of screening with increasing valence (e.g. the loss of the s^2 screening between the In^{1+} and In^{3+} states). The systematic WL-intensity increase, between $In-InCl-InCl_3$, is clear. The WL-intensity in the In_2O_3 is also enhanced by an amount somewhat more than in $InCl_3$ indicating bonding/ligand dependence. It is important to note that the WL intensity of $Cs_{1.17}In_{0.81}Cl_3$ is intermediate between the In^{1+} and In^{3+} standards (the sizable ligand/structure dependence in the In^{3+} standards is qualification to this statement). The plot of the Gaussian fitted WL-areas versus In formal valence, for the standard compounds (referred to above) is shown in Fig. 8 along with a linear fit to the standard area data. Within the non-negligible uncertainties in these estimates these results supports the average valence in $Cs_{1.17}In_{0.81}Cl_3$ lying in the vicinity of In^{2+}.
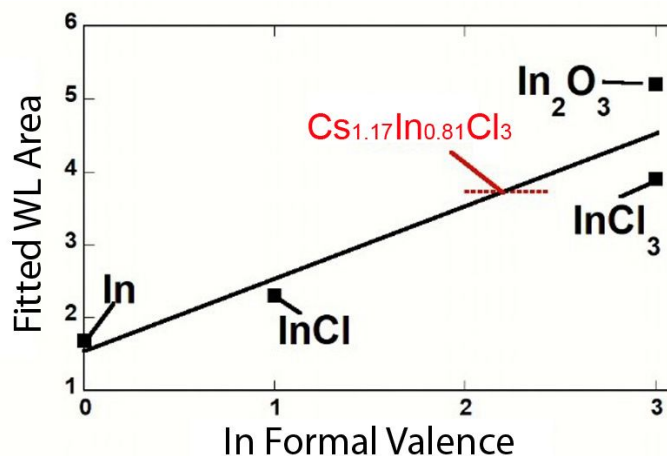
Figure 8. A plot of the Gaussian fitted WL-area/intensity vs formal In valence for the In-K edge standard spectra in Figure 7b. The solid line is a linear fit to the standard spectra data. The fitted WL-Area for $Cs_{1.17}In_{0.81}Cl_3$ is indicated by a dashed red line crossing the standard fitted-line.

As another check on the charge separation on the sites in $Cs_{1.17}In_{0.81}Cl_3$, FEFF 8.4 model[45] calculations for all of the sites was performed with the near edge results being shown in Fig. 7b. In view of the substantial uncertainty in absolute energy in such modeling the results have been presented relative to the calculated all-site-average peak for $Cs_{1.17}In_{0.81}Cl_3$. The determined structure was used in this modeling. The model calculations indicate: the In2 and In4 sites have a smaller chemical shift, and smaller WL-area consistent with a smaller In-valence; the In1 and In3 sites have a larger chemical shift, and larger WL-area consistent with a larger In-valence. Thus, the model results are consistent with the experimental observations. It is worth noting that charge separation in solids can often be smaller than the stable full integral valence differences.

Raman Spectroscopy. To further compare $Cs_{1.17}In_{0.81}Cl_3$ with $CsTlCl_3$ and $CsTl_{1-x}Hg_xCl_3$ ($0 \leq x < 1$),[17, 49] the Raman spectrum of $Cs_{1.17}In_{0.81}Cl_3$ is collected at room temperature under ambient pressure (Fig. 9). For cubic $CsTlCl_3$, the calculated phonon frequency of Tl-Cl stretching mode of cubic $CsTlCl_3$ is 277 cm^{-1}. The experimental Raman spectra of both cubic ($Fm\overline{3}m$) and tetragonal $CsTlCl_3$ ($I4/m$) show the major phonon frequency at 270 cm^{-1}, in agreement with the theoretical calculation results.[17] In $CsTl_{1-x}Hg_xCl_3$, active Raman Tl^+-Cl-Tl^{3+} modes are also observed around 270 cm^{-1}.[49] Here, the major phonon frequency of $Cs_{1.17}In_{0.81}Cl_3$ is at 278 cm^{-1}, which is close to values of Raman for Tl^+-Cl-Tl^{3+} modes in $CsTlCl_3$ and $CsTl_{1-x}Hg_xCl_3$. Based on the similarity observed in the structure and Raman spectra between $Cs_{1.17}In_{0.81}Cl_3$, $CsTlCl_3$ and $CsTl_{1-x}Hg_xCl_3$, the active Raman mode observed in $Cs_{1.17}In_{0.81}Cl_3$ can be ascribed to In^+-Cl-In^{3+}.
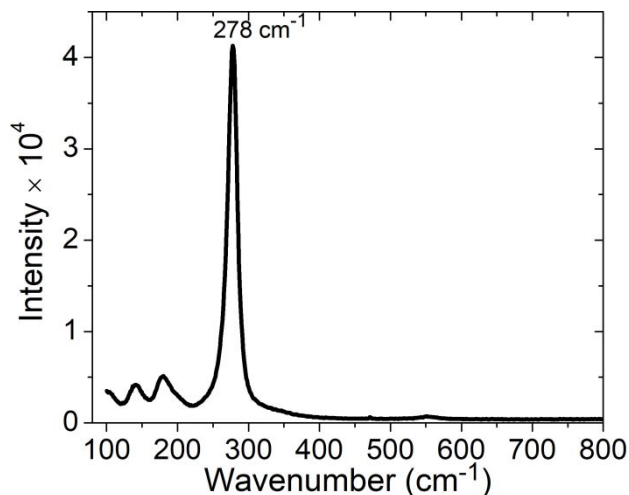
Figure 9. Raman spectrum of $Cs_{1.17}In_{0.81}Cl_3$ ((λ_{exc} = 532nm).

DFT calculations. To gain insight of the band structure and estimate the band gap, first-principles DFT calculations were carried out with both GGA (PBE version) and mBJ approaches (Fig. 10). The calculations were conducted on $CsInCl_3$ version of structural model I, *i.e.*, without considering the apparent presence of Cs in the In sites or attendant vacancies in the crystal structure of $Cs_{1.17}In_{0.81}Cl_3$. The band structure with GGA approaches the lowest energy of the conduction band located at the N point, while the highest energy of valence band is located at the X point, respectively, which indicates an indirect band gap of 2.27 eV (Fig. 10a).

As shown in Fig. 10, the valence band near the density of states (DOS) around the Fermi level is mostly contributed by the In states, but the strong peaks locating at lower energy are dominated by Cl states (Fig. 10a-b, d-e). The In2 (1+, $5s^2$) and In4 (1+, $5s^2$) $5s$ bands locate in valence bands, while In1 (3+, $5s^0$) and In3 (3+, $5s^0$) $5s$ bands locate in conduction bands, which clearly support the two oxidation states in the structure as revealed in the structure and XANES analysis. A broader computational survey of compounds $AInX_3$ (A = alkali metals, X = F or Cl) predicts that the most stable state of $CsInCl_3$, l3 has a single In^{2+} site, but that it is only slightly more likely to occur than the phase described in this work (Table S2, S3).[16]
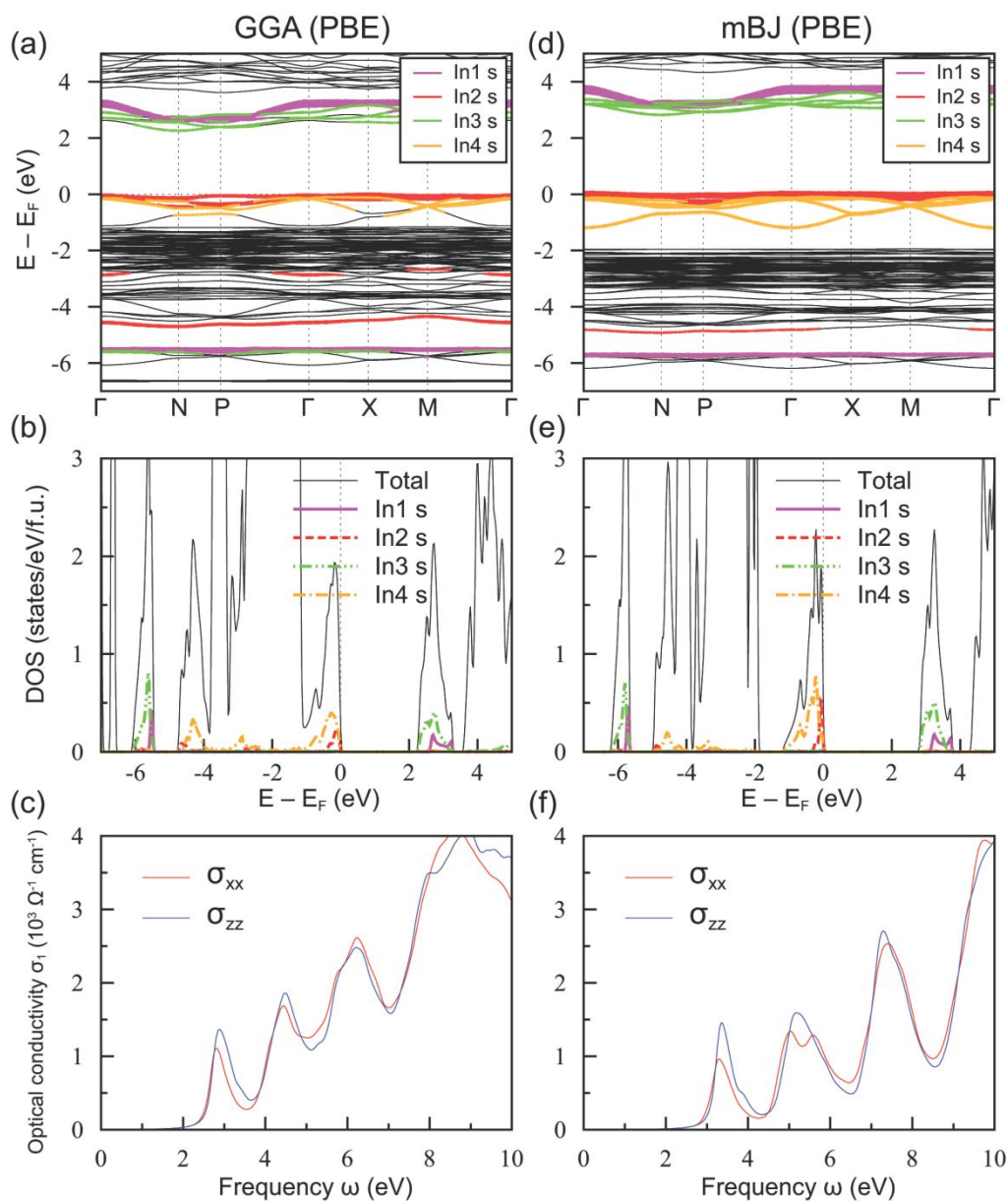
Figure 10. Band structure, density of states, and calculated optical conductivity of $CsInCl_3$ with GGA (a, b, c) and mBJ (d, e, f).

The GGA calculated corresponding optical conductivity predicts an optical gap of 2.42 eV (Fig. 10c). In comparison with the GGA results, the calculated band structure using mBJ shows similar indirect band gap features, but with a larger band gap of 2.83 eV (Fig 10.d-f). In the valence bands, these strong peaks are shifted to lower energy. Consequently, the calculated optical gap using mBJ approach is increased to 3.03 eV. The calculated band gap here, is much larger than the literature report (< 1 eV) of theoretical $CsInCl_3$.[15] Since our calculations are carried out based on the experimental crystal structure, the estimated band gap shown here is more reliable than the reported values.[14-15] The total DOS and estimated optical band gap of $CsInCl_3$ are similar to those of $CsTlCl_3$,[17] which is predicted to exhibit superconductivity with proper doping. Therefore, it is worth carrying out further calculations and corresponding experiments on

14

CsInCl$_3$ to explore the possibility of making it superconducting by design. It seems especially promising to seek to dope this material, in view of its apparent natural tendency to prefer off stoichiometry. However, determining and controlling the charge state in sample preparation may be a significant challenge.

Conclusions

While CsInCl$_3$ was originally predicted to be a perovskite, synchrotron X-ray diffraction data and x-ray fluorescence measurements show that the stable material has some Cs in the nominal In sites, and adopts a tetragonal perovskite-related phase (I4/m) of composition Cs$_{1.17}$In$_{0.81}$Cl$_3$, with both corner-sharing and edge-sharing InCl6 octahedra and InCl7 pentagonal bipyramids. Cs$_{1.17}$In$_{0.81}$Cl$_3$ is isostructural with tetragonal CsTlCl$_3$, which was predicted to be a superconductor with proper doping. The revealed oxidation state of In is not 2+, as the theory predicted, but with a charge-ordering of In$^+$ and In^{3+} on four crystallographic positions in the structure. This is a rare inorganic compound accommodating both In$^+$ and In^{3+} in a nominally double perovskite derived "Cs$_2$In$^+$In^{3+}Cl$_6$" structure. The mixed valence of In$^+$ and In^{3+} is confirmed by detailed X-ray absorption spectroscopy. Raman spectroscopy demonstrates the In$^+$-Cs-In^{3+} active mode with phonon frequency of 278 cm^{-1}, similar to that of the Tl$^+$-Cs-Tl^{3+} stretching modes in CsTlCl$_3$ and CsTl$_{1-x}$Hg$_x$Cl$_3$. Theoretical calculations conducted on the In-deficient CsIn$_{0.996}$Cl$_3$ indicate that it is an indirect band gap semiconductor with a band gap of ~ 2.27 eV. The large indirect bandgap suggests that this nonstoichiometric perovskite derived phase is not a good candidate for photovoltaic application. The experimental results, however, provide a basis for future theoretical calculations for designing related inorganic halide perovskites for potential photovoltaic functions, or superconductivity.

Acknowledgements

Supporting Information

EDX spectrum of Cs$_{1.17}$In$_{0.81}$Cl$_3$ sample; tilt series of SAED patterns around the c-axis; refined crystallographic data of model I without Cs in In sites; fractional occupancies of sites In2 and In4 as defined by Rietveld refinements of the SXPD; DFT calculation of theoretical and experimental crystal structures of Cs$_{1.17}$In$_{0.81}$Cl$_3$ with space group *I4/m*; DFT calculation of Hull energy, energy difference, and existence probability for theoretical and experimental crystal structures of CsInCl$_3$; Cs1$_{.17}$In$_{0.81}$Cl$_3$ cif file.

References

1. Liang, J.; Wang, C.; Wang, Y.; Xu, Z.; Lu, Z.; Ma, Y.; Zhu, H.; Hu, Y.; Xiao, C.; Yi, X.; Zhu, G.; Lv, H.; Ma, L.; Chen, T.; Tie, Z.; Jin, Z.; Liu, J., All-Inorganic Perovskite Solar Cells. *J. Am. Chem. Soc.* **2016**, *138*, 15829-15832.

2. Jeong, B.; Han, H.; Choi, Y. J.; Cho, S. H.; Kim, E. H.; Lee, S. W.; Kim, J. S.; Park, C.; Kim, D.; Park, C., All-Inorganic $CsPbI_3$ Perovskite Phase-Stabilized by Poly(ethylene oxide) for Red-Light-Emitting Diodes. *Adv. Func. Mater.* **2018**, 28, 1706401.

3. Han, J. S.; Le, Q. V.; Choi, J.; Hong, K.; Moon, C. W.; Kim, T. L.; Kim, H.; Kim, S. Y.; Jang, H. W., Air-Stable Cesium Lead Iodide Perovskite for Ultra-Low Operating Voltage Resistive Switching. *Adv. Func. Mater.* **2018**, *28*, 1705783.

4. Vargas, B.; Ramos, E.; Perez-Gutierrez, E.; Alonso, J. C.; Solis-Ibarra, D., A Direct Bandgap Copper-Antimony Halide Perovskite. *J. Am. Chem. Soc.* **2017**, *139*, 9116-9119.

5. Volonakis, G.; Haghighirad, A. A.; Milot, R. L.; Sio, W. H.; Filip, M. R.; Wenger, B.; Johnston, M. B.; Herz, L. M.; Snaith, H. J.; Giustino, F., $Cs_2InAgCl_6$: A New Lead-Free Halide Double Perovskite with Direct Band Gap. *J. Phys. Chem. Lett.* **2017**, *8*, 772-778.

6. Filip, M. R.; Eperon, G. E.; Snaith, H. J.; Giustino, F., Steric Engineering of Metal-halide Perovskites with Tunable Optical Band Gaps. *Nat. Comm.* **2014**, *5*, 5757.

7. He, X. X.; Liu, P.; Zhang, H. H.; Liao, Q.; Yao, J. N.; Fu, H. B., Patterning Multicolored Microdisk Laser Arrays of Cesium Lead Halide Perovskite. *Adv. Mater.* **2017**, *29*, 1604510.

8. Amgar, D.; Aharon, S.; Etgar, L., Inorganic and Hybrid Organo-Metal Perovskite Nanostructures: Synthesis, Properties, and Applications. *Adv. Func. Mater.* **2016**, *26*, 8576-8593.

9. Kovalenko, M. V.; Protesescu, L.; Bodnarchuk, M. I., Properties and Potential Optoelectronic Applications of Lead Halide Perovskite Nanocrystals. *Science* **2017,** *358*, 745-750.

10. Swarnkar, A.; Marshall, A. R.; Sanehira, E. M.; Chernomordik, B. D.; Moore, D. T.; Christians, J. A.; Chakrabarti, T.; Luther, J. M., Quantum Dot-Induced Phase Stabilization of Alpha-CsPbI$_3$ Perovskite for High-Efficiency Photovoltaics. *Science* **2016**, *354*, 92-95.

11. Liang, J.; Zhao, P.; Wang, C.; Wang, Y.; Hu, Y.; Zhu, G.; Ma, L.; Liu, J.; Jin, Z., CsPb$_{0.9}$Sn$_{0.1}$IBr$_2$ Based All-Inorganic Perovskite Solar Cells with Exceptional Efficiency and Stability. *J. Am. Chem. Soc.* **2017**, *139*, 14009-14012.

12. Sanehira, E. M.; Marshall, A. R.; Christians, J. A.; Harvey, S. P.; Ciesielski, P. N.; Wheeler, L. M.; Schulz, P.; Lin, L. Y.; Beard, M. C.; Luther, J. M., Enhanced Mobility CsPbI$_3$ Quantum Dot Arrays for Record-Efficiency, High-Voltage Photovoltaic Cells. *Sci. Adv.* **2017**, *3*, eaao4204.

13. Zhang, L.; Yang, X.; Jiang, Q.; Wang, P.; Yin, Z.; Zhang, X.; Tan, H.; Yang, Y. M.; Wei, M.; Sutherland, B. R.; Sargent, E. H.; You, J., Ultra-Bright and Highly Efficient Inorganic Based Perovskite Light-Emitting Diodes. *Nat. Comm.* **2017**, *8*, 15640.

14. Filip, M. R.; Giustino, F., Computational Screening of Homovalent Lead Substitution in Organic–Inorganic Halide Perovskites. *J. Phys. Chem. C* **2015**, *120*, 166-173.

15. Körbel, S.; Marques, M. A. L.; Botti, S., Stability and Electronic Properties of New Inorganic Perovskites from High-Throughput Ab Initio Calculations. *J. Mater.Chem. C* **2016**, *4*, 3157-3167.

16. Kang, C.-J., Kotliar, G., Material Desing of Indium Based Compounds: Possible Candidates for Charge, Valence, and Bond Disproportionation and Superconductivity. *Phys. Rev. Materials*, **2019**, *3*, 015001.

17. Retuerto, M.; Emge, T.; Hadermann, J.; Stephens, P. W.; Li, M. R.; Yin, Z. P.; Croft, M.; Ignatov, A.; Zhang, S. J.; Yuan, Z.; Jin, C.; Simonson, J. W.; Aronson, M. C.; Pan, A.; Basov, D. N.; Kotliar, G.; Greenblatt, M., Synthesis and Properties of Charge-Ordered Thallium Halide Perovskites, CsTl$^+_{0.5}$Tl$^{3+}_{0.5}$X$_3$ (X = F or Cl): Theoretical Precursors for Superconductivity? *Chem. Mater.* **2013**, *25*, 4071-4079.

18.   Cava, R. J.; Batlogg, B.; Krajewski, J. J.; Farrow, R.; Rupp, L. W.; White, A. E.; Short, K.; Peck, W. F.; Kometani, T., Superconductivity near 30 K Without Copper - the $Ba_{0.6}K_{0.4}BiO_3$ Perovskite. *Nature* **1988**, *332*, 814-816.

19.   Climent-Pascual, E.; Ni, N.; Jia, S.; Huang, Q.; Cava, R. J., Polymorphism in $BaPb_{1-x}Bi_xO_3$ at the Superconducting Composition. *Phys. Rev. B: Condens. Matter Mater. Phys.* **2011**, *83*, 174512.

20.   Yin, Z. P.; Kutepov, A.; Kotliar, G., Correlation-Enhanced Electron-Phonon Coupling: Applications of GW and Screened Hybrid Functional to Bismuthates, Chloronitrides, and Other High-Tc Superconductors. *Phys. Rev. X* **2013**, *3*, 021011.

21.   Yin, Z. P.; Kotliar, G., Rational Material Design of Mixed-Valent High-Tc Superconductors. *EPL* **2013**, *101*, 27002.

22.   Coehlo, A. A, Topas-Academic V6, http://www.topas-academic.net (accessed February 17, 2019).

23.   Segre, C.U.; Leyarovska, N. E.; Chapman, L.D.; Lavender, W.M.; Plag, P.W.; King, A.S.; Kropf, A.J.; Bunker, B.A.; Kemner, K.M.; Dutta,P.; Duran, R.S.; Kaduk, J. The MRCAT Insertion Device Beamline at the Advanced Photon Source. *CP521, Synchrotron Radiation Instrumentation: Eleventh U.S. National Conference*, P. Pianetta, et al., Eds. American Insitute of Physics: New York, **2000**, pp 419-422.

24.   Newville, B. R. a. M., ATHENA, ARTEMIS, HEPHAESTUS: Data Nnalysis for X-ray Absorption Spectroscopy Using IFEFFIT. *J. Synchrotron Rad.* **2005**, *12*, 537-541.

25.   Newville, M., IFEFFIT: Interactive EXAFS Analysis and FEFF Fitting. *J. Synchrotron Rad.* **2001**, *8*, 322-324.

26.   Wojdyr, M., Fityk: a General-Purpose Peak Fitting Program. *J. Appl. Cryst.* **2010,** *43*, 1126-1128.

27.   Blaha, P. S., K.; Madsen, G. K. H.; Kvasnicka, D.; Luitz, J., *WIEN2K, An Augmented Plane Wave + Local Orbitals Program for Calculating Crystal Properties*. Technische Universität Wien: Wien: Austria, **2001**.

28.   Perdew, J. P.; Burke, K.; Ernzerhof, M., Generalized Gradient Approximation Made Simple. *Phy. Rev. Lett.* **1996**, *77*, 3865-3868.

29.   Camargo-Martínez, J. A.; Baquero, R., Performance of the Modified Becke-Johnson Potential for Semiconductors. *Phys. Rev. B: Condens. Matter Mater. Phys.* **2012**, *86*, 195106.

30.   Brown, I. D., Recent Developments in the Methods and Applications of the Bond Valence Model. *Chem. Rev.* **2009**, *109*, 6858-6919.

31.   Meyer, B. G., $A_3In_2Cl_9$ (A = Cs, Rb, In, Tl) and $Cs_3In_2Br_{9-x}Cl_x$ (x = 0, 3, 6, 7, 8). *Z. Anorg. Allg. Chem.* **1978**, *445*, 140-146.

32.   Solans, X., Structures of $Rb_2[InCl_5(H_2O)]$ and $Rb_2[InCl_5(H_2O)]$. *Acta Cryst.* **1988**, *C44*, 965-967.

33.   Van Der Vorst, C. P. J. M., Verschoor, G. C.; Maaskant, W. J. A., The Structures of Yellow and Red Indium Monochloride. *Acta Cryst.* **1978**, *B34*, 3333-3335.

34.   Meyer, V. G. B., R., New Investigations into Mixed-Valence Indium(I, III) Chlorides: The Phase Diagram In/Cl in the 30-50 mole % In Range and the Crystal Structure of In_5Cl_9. *Z. Anorg. Allg. Chem.* **1983**, *503*, 126-132.

35.   Dronskowski, R., Chemical Bonding of the Binary Indium Bromides. *Inorg. Chem.* **1994**, *33*, 6201-6212.

36.   Dronskowski, R., InFeBr3 and InMnBr3 - Synthesis, Crystal-Structure, Magnetic-Properties, and Electronic Structure. *Inorg. Chem.* **1994**, *33*, 5927-5933.

37.   Dronskowski, R., $In_3Ti_2Br_9$: Jahn-Teller Unstable Indium(I) and Antiferromagnetically Coupled Titanium(Iii) Atoms. *Chem. Eur. J.* **1995**, *1*, 118-123.

38.   Howard, C. J. K., B. J.; Woodward, P. M., Ordered Double Perovskites - a Group-Theoretical Analysis. *Acta Cryst.* **2003**, *B59*, 463-471.

39.   Javier Zúñiga, F.; Tressaud, A.; Darriet, J., The Low-Temperature form of Rb_2KCrF_6 and Rb_2KGaF_6: The First Example of an Elpasolite-Derived Structure with Pentagonal Bipyramid in the B-Sublattice. *J. Solid State Chem.* **2006**, *179*, 3607-3614.

40.   Abakumov, A. M.; King, G.; Laurinavichute, V. K.; Rozova, M. G.; Woodward, P. M.; Antipov, E. V., The Crystal Structure of Alpha-K_3AlF_6: Elpasolites and Double Perovskites with Broken Corner-Sharing Connectivity of the Octahedral Framework. *Inorg. Chem.* **2009**, *48*, 9336-9344.

41.   King, G.; Abakumov, A. M.; Woodward, P. M.; Llobet, A.; Tsirlin, A. A.; Batuk, D.; Antipov, E. V., The high-temperature polymorphs of K_3AlF_6. *Inorg. Chem.* **2011**, *50*, 7792-801.

42.   King, G.; Abakumov, A. M.; Hadermann, J.; Alekseeva, A. M.; Rozova, M. G.; Perkisas, T.; Woodward, P. M.; Van Tendeloo, G.; Antipov, E. V., Crystal Structure and Phase Transitions in Sr_3WO_6. *Inorg. Chem.* **2010,** *49*, 6058-6065.

43.   Stoger, B.; Weil, M.; Zobetz, E., Sr_3TeO_6 and Ba_3TeO_6: Double Perovskites with Pronounced Superstructures. *Z Kristallogr.* **2010,** *225*, 125-138.

44.   Fry, A. M.; Woodward, P. M., Structures of α-$K_3MoO_3F_3$ and α-$Rb_3MoO_3F_3$: Ferroelectricity from Anion Ordering and Noncooperative Octahedral Tilting. *Cryst. Growth. Des.* **2013,** *13*, 5404-5410.

45.   Mandal, T. K.; Poltavets, V. V.; Croft, M.; Greenblatt, M., Synthesis, Structure and Magnetic Properties of $A_2MnB'O6$ (A = Ca, Sr; B' = Sb, Ta) Double Perovskites. *J. Solid State Chem.* **2008,** *181*, 2325-2331.

46.   Ankudinov, A. L.; Ravel, B.; Rehr, J. J.; Conradson, S. D., Real Space Multiple-Scattering Calculation and Interpretation of X-Ray-Absorption Near-Edge Structure, **1998,** *58*, 7565.

47.   Yang, T.; Perkisas, T.; Hadermann, J.; Croft, M.; Ignatov, A.; Van Tendeloo, G.; Greenblatt, M., Synthesis and Structure Determination of Ferromagnetic Semiconductors $LaAMnSnO_6$(A = Sr, Ba). *J. Mater. Chem.* **2011**, *21*, 199-205.

48.   Li, M.-R.; Retuerto, M.; Bok Go, Y.; Emge, T. J.; Croft, M.; Ignatov, A.; Ramanujachary, K. V.; Dachraoui, W.; Hadermann, J.; Tang, M.-B.; Zhao, J.-T.; Greenblatt, M., Synthesis, Crystal Structure, and Properties of $KSbO_3$-type $Bi_3Mn_{1.9}Te_{1.1}O_{11}$. *J. Solid State Chem.* **2013**, *197*, 543-549.

49.   Retuerto, M.; Yin, Z.; Emge, T. J.; Stephens, P. W.; Li, M. R.; Sarkar, T.; Croft, M. C.; Ignatov, A.;

Yuan, Z.; Zhang, S. J.; Jin, C.; Paria Sena, R.; Hadermann, J.; Kotliar, G.; Greenblatt, M., Hole Doping and

Structural Transformation in $CsTl_{1-x}Hg_xCl_3$. *Inorg. Chem.* **2015**, *54*, 1066-75.

Table of Contents Graphic